Check for updates

Slow magnetisation relaxation in tetraoxolene-bridged rare earth complexes†

Maja A. Dunstan, [ID] [a] Elodie Rousset, [ID] [a] Marie-Emmanuelle Boulon, [ID] [b] Robert W. Gable, [ID] [a] Lorenzo Sorace [ID] [b] and Colette Boskovic [ID] *[a]

Three families of tetraoxolene-bridged dinuclear rare earth (RE) complexes have been synthesised and characterised, with general formula [((HB(pz)$_3$)$_2$RE)$_2$(μ-tetraoxolene)] (HB(pz)$_3^-$ = hydrotris(pyrazolyl) borate; tetraoxolene = chloranilate (**1-RE**), the dianionic form of 2,5-dihydroxy-1,4-benzoquinone (**2-RE**), or its 3,6-dimethyl analogue (**3-RE**)). In each case, the bridging tetraoxolene ligand is in the diamagnetic dianionic form and species with selected lanthanoid(III) ions from Eu(III) to Yb(III) have been obtained, as well as the diamagnetic Y(III) analogues. Use of the 3,6-dimethyl substituted tetraoxolene ligand (Me$_2$-dhbq^{2-}) has also afforded the two byproducts [((HB(pz)$_3$)(MeOH)(B(OMe)$_4$)Y)$_2$(μ-Me$_2$dhbq)] (**4-Y**) and [{((HB(pz)$_3$)(MeOH)Y)$_2$(μ-B(OMe)$_4$)}$_2$(μ-Me$_2$dhbq)$_2$]Cl$_2$ (**5-Y**), with the B(OMe)$_4^-$ ligands arising from partial decomposition of HB(pz)$_3^-$. Electrochemical studies on the soluble **1-RE** and **3-RE** families indicate multiple tetraoxolene-based redox processes. Magnetochemical and EPR studies of **3-Gd** indicate the negligible magnetic coupling between the two Gd(III) centres through the diamagnetic tetraoxolene bridge. Alternating current magnetic susceptibility studies of **1-Dy** and **3-Dy** reveal slow magnetic relaxation, with quantum tunnelling of the magnetisation (QTM) dominant in the absence of an applied dc field. The application of a dc field suppresses the QTM and relaxation data are consistent with an Orbach relaxation mechanism playing a major role in both cases, with effective energy barriers to magnetisation reversal determined as 47 and 24 K for **1-Dy** and **3-Dy**, respectively. The different dynamic magnetic behaviour evident for **1-Dy** and **3-Dy** arises from small differences in the local Dy(III) coordination environments, highlighting the subtle structural effects responsible for the electronic structure and resulting magnetic behaviour.

*[a]School of Chemistry, University of Melbourne, Parkville, Victoria, 3010, Australia.
E-mail: c.boskovic@unimelb.edu.au*
*[b]UdR INSTM and Department of Chemistry "U. Schiff", University of Florence,
50019 Sesto Fiorentino, FI, Italy*
†Electronic supplementary information (ESI) available: Additional structural
representations, spectroscopic and magnetic data. CCDC 1566106–1566112. For
ESI and crystallographic data in CIF or other electronic format see DOI: 10.1039/
c7dt02932b

Introduction

The last few years have seen impressive advances in the field of single-molecule magnets (SMMs), with slow magnetic relaxation that arises from intrinsic molecular properties reported at unprecedentedly high temperatures.[1–5] Two recent spectacular examples are mononuclear Dy complexes with high axial symmetry, each with experimentally measured energy barriers to magnetisation reversal (U_{eff}) over 1200 cm^{-1} (1700 K).[1,2] A salt of the complex [(Cp^{ttt})Dy]$^+$ (Cp^{ttt} = 1,2,4-tri(*tert*-butyl)cyclopentadienide) exhibits magnetisation hysteresis up to 60 K.[1] Thus the practical target of molecules that can act as magnets at liquid nitrogen temperatures for applications,

for example in molecular spin valves and spin transistors, seems closer to reality than ever. Before such applications can be realised, it must become possible to deposit the molecules onto a surface or otherwise incorporate them into a matrix in such a way that the SMM properties are maintained and the molecules can be addressed individually, for instance *via* a magnetic STM tip. Advances in these areas of SMM deposition and addressing are also being vigorously pursued.[6–11]

The energy barrier to magnetisation reversal for lanthanoid (Ln) SMMs arises from crystal field (CF) splitting of the ground spin–orbit coupled *J* state of the Ln(III) ion into microstates. The relative order, energies and m_J composition of these states depend on the local symmetry and CF of the Ln(III) ion.[12] In situations where the CF splitting affords a bistable ground state, with dominant contributions from large m_J values and large energy separations between the microstates, an energy barrier to magnetisation reversal gives rise to the slow magnetic relaxation that is a signature of SMMs. For lanthanoid SMMs, magnetisation relaxation typically occurs through the first few higher energy microstates. Quantum tunnelling of the magnetisation (QTM) between degenerate microstates is an efficient relaxation pathway for many Ln-SMMs,[13,14] although

the application of an external field can suppress the QTM, as it removes the degeneracy of the microstates involved.[15] Dysprosium(III) features most prominently in Ln-SMMs due to its potentially high magnetic anisotropy and Kramers nature that affords a doubly degenerate ground state.[16–20]

Efforts to improve SMM properties by incorporating more than one lanthanoid(III) ion in polynuclear complexes have also been fruitful.[16,21–23] The intrinsically small exchange coupling between Ln(III) ions can often mean that the different ions act as discrete non-interacting magnetic units within polynuclear complexes. Nevertheless, several examples demonstrate how the ground state magnetic moment and/or magnetic anisotropy, and therefore U_{eff}, can be enhanced by linking lanthanoid(III) ions through bridging ligands in dinuclear or polynuclear complexes.[24–27] As a further advantage, the weak exchange interactions in these systems provides an effective small bias field, which can result in suppression of the QTM in zero external applied field that can prohibit bistability. These examples generally rely on the specific coordination mode of the ligand bridge enforcing ferromagnetic coupling or alignment of the individual local anisotropy axes.

The use of paramagnetic radical ligands to bridge two lanthanoid(III) ions can have a significant impact on the resulting SMM properties. The paramagnetic ligand can mediate exchange coupling, enhancing the magnetic ground state of the molecule, as well as offering a means for suppressing zero-field QTM. The most notable example is the radical bridged complex $[\{((Me_3Si)_2N)_2(THF)Tb\}_2(\mu-\eta^2:\eta^2-N_2)]$, which exhibits hysteresis at 14 K.[28] Other dinuclear lanthanoid SMMs incorporating radical bridging ligands employ bipyrimidyl, indigo or tetrathiafulvalene ligands.[29–32] Of particular interest is a recently reported $[(Dy(tmhd)_3)_2(\mu-bptz)]^{n-}$ complex (tmhd$^-$ = 2,2,6,6-tetramethyl-3,5-heptanedionate, bptz^{n-} = 3,6-bis(2-pyridyl)-1,2,4,5-tetrazine, n = 0, 1), which can be isolated with the bptz^{n-} either as a radical or diamagnetic ligand.[33] Both complexes are SMMs; however, the complex with the reduced radical bridging ligand exhibits intramolecular ferromagnetic coupling and no QTM at zero-field.

Potentially interesting for the possibility of accessing radical oxidation states to bridge lanthanoid(III) ions are tetraoxolene-based ligands, which commonly exist in the closed shell dianionic and radical trianionic forms (Chart 1).[34,35] Several chloranilate-bridged dinuclear lanthanoid(III) complexes $[((HB(pz)_3)_2Ln)_2(\mu-ca)]$ (HB(pz)$_3^-$ = hydrotris(pyrazolyl) borate; ca^{2-} = chloranilate, Chart 1) have been reported previously, however no magnetic studies were performed.[36] In this

work we report our efforts in the synthesis and structural and magnetochemical characterisation of 24 complexes in three structural families of formula $[((HB(pz)_3)_2RE)_2(\mu-tetraoxolene)]$, where the bis-bidentate tetraoxolene ligand (Chart 1) is the dianionic form of 2,5-dihydroxy-1,4-benzoquinone (dhbq^{2-}), its 3,6-dimethyl analogue (Me$_2$dhbq^{2-}) or chloranilate (ca^{2-}). At the outset of this work, our aim was also to explore the redox-chemistry with a view to ultimately accessing dinuclear complexes incorporating a radical form of the bridging ligand to potentially optimise any SMM behaviour.

Results and discussion

Synthesis

The rare earth (RE) complexes $[((HB(pz)_3)_2RE)_2(\mu-ca)]$ (**1-RE**) with RE = Y, Eu, Gd, Tb, Dy, Ho, Er and Yb were synthesised following modification of the literature procedure to enhance the purity of the product.[36] Four equivalents of KHB(pz)$_3$ were added to a stirred ethanol/dichloromethane solution containing two equivalents of rare earth salt. Slightly less than one equivalent of the caH$_2$ ligand was doubly deprotonated with Et$_3$N and added dropwise to an unstirred suspension of the rare earth mixture and swirled gently, causing dissolution of the suspension. A fine white solid precipitated, which was removed by filtration and the purple filtrate left to stand, affording a crystalline sample of **1-RE**. The elemental analysis reported previously for these compounds indicated that the bulk samples are often impure,[36] which we have been able to overcome by multiple recrystallisations from dichloromethane/ n-hexane to access analytically pure samples of **1-RE·2CH$_2$Cl$_2$** in 20–50% yield. A single crystal of another solvate, **1-Y·2Me$_2$CO**, was also obtained by recrystallisation from acetone/ n-hexane. The complexes $[((HB(pz)_3)_2RE)_2(\mu-dhbq)]$ (**2-RE**) with RE = Y, Eu, Gd, Tb, Dy, Ho, Er and Yb were synthesised as per **1-RE**, however the pink microcrystalline products are highly insoluble and cannot be purified by recrystallisation. The crude yields of these complexes were in the range 58–76%. The purple complexes $[((HB(pz)_3)_2RE)_2(\mu-Me_2dhbq)]$ (**3-RE**) with RE = Y, Eu, Gd, Tb, Dy, Ho, Er and Yb were synthesised in a manner analogous to that employed for **1-RE** and obtained in generally slightly higher yields of 43–49%. Of the three families of compounds, **3-RE** is the easiest to purify, with a single recrystallisation from dichloromethane/n-hexane affording analytically pure products of **3-RE·xCH$_2$Cl$_2$** (x = 0–2). Both the **1-RE** and **3-RE** dinuclear complexes undergo some decomposition in alcoholic solutions and as such the crude products were rapidly isolated from the ethanol-containing reaction solution prior to recrystallisation. Powder X-ray diffraction data (Fig. S1†) measured for the bulk samples of **1-RE·2CH$_2$Cl$_2$**, **2-RE** and **3-RE·xCH$_2$Cl$_2$** (RE = Y, Eu, Gd, Tb, Dy, Ho, Er and Yb) are in good agreement with diffractograms calculated from the single crystal structures of the three families, supporting the composition of the bulk samples. Elemental analysis confirms the purity of the samples of **1-Dy·2CH$_2$Cl$_2$** and **3-RE·xCH$_2$Cl$_2$** (**3-Gd**·2CH$_2$Cl$_2$, **3-Tb**·0.7CH$_2$Cl$_2$
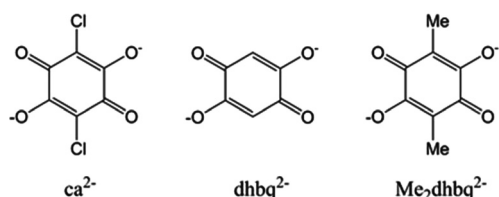
Chart 1 Tetraoxolene ligands used in this work.

and 3-Dy·1.1CH₂Cl₂), for which magnetochemical data are reported herein. Thermogravimetric analysis (Fig. S2†) of these compounds are consistent with the dichloromethane solvation suggested by elemental analysis and integration of the ^{1}H NMR spectra (Fig. S3†) of diamagnetic 1-Y·2CH₂Cl₂ and 3-Y·1.2CH₂Cl₂ confirms the extent of dichloromethane solvation.

Two other complexes of interest formed reproducibly as byproducts during initial efforts to synthesise 3-Y. The compounds [((HB(pz)₃)(MeOH)(B(OMe)₄)Y)₂(μ-Me₂dhbq)] (4-Y) and [{((HB(pz)₃)(MeOH)Y)₂μ-(B(OMe)₄)}₂(μ-Me₂dhbq)₂]Cl₂ (5-Y) are obtained when the synthesis of 3-Y is attempted in methanol; 4-Y in the refrigerator, and 5-Y in the freezer. Large well-formed crystals of compounds containing these complexes were manually separated from 3-Y for X-ray structural analysis, but it has not been possible to obtain pure bulk samples for further study. Both 4-Y and 5-Y incorporate B(OMe)₄⁻ ligands that form *in situ* from reaction of the HB(pz)₃⁻ with methanol. Similar reactivity of tris- and bis-pyrazolylborates with alcohols has been observed previously.[37–39]

Structure descriptions

The single-crystal X-ray data for seven representative compounds: 1-Y·2Me₂CO, 1-Y·2CH₂Cl₂, 1-Dy·2CH₂Cl₂, 2-Y, 3-Y·1.2CH₂Cl₂, 4-Y·3.5MeOH and 5-Y·5MeOH, are presented in Table 1. These compounds are representative of the five structural families and two different solvates of 1-Y, as well as a Dy analogue to indicate the isomorphism upon varying the rare earth metal. Compound 1-Y·2Me₂CO crystallises as purple needles in the monoclinic space group P2₁/n, with half a dinuclear complex as well as one solvent molecule per asymmetric unit. Isomorphous compounds 1-Y·2CH₂Cl₂ and 1-Dy·2CH₂Cl₂ crystallise as purple parallelogram-shaped plates in the monoclinic space group P2₁/n, with half a complex and a solvent molecule per asymmetric unit. Compounds 1-Y·2Me₂CO, 1-Y·2CH₂Cl₂, 1-Dy·2CH₂Cl₂ are also isomorphous with previously reported 1-Yb, which is reported to crystallise solvent-free.[36] Compound 2-Y crystallises as small pink needles in the monoclinic space group P2₁/n with half a dinuclear complex per asymmetric unit with no solvent. Compound 3-Y·1.2CH₂Cl₂ crystallises as clusters of fine purple needles in the trigonal space group R3̄, with one dinuclear complex per asymmetric unit plus solvent.

The neutral dinuclear rare earth complexes in 1-Y·2Me₂CO, 1-Y·2CH₂Cl₂, 1-Dy·2CH₂Cl₂, 2-Y, 3-Y·1.2CH₂Cl₂ are isostructural (Fig. 1), allowing for the different substituents on the bridging tetraoxolene ligands. The rare earth centres are all eight coordinate with a {N₆O₂} coordination sphere arising from coordination to two tripodal HB(pz)₃⁻ ligands and the bis-bidentate tetraoxolene bridging ligand. The rare earth coordination geometries are closest to either square antiprismatic (2-Y, 3-Y·1.2CH₂Cl₂) or triangular dodecahedral (1-Y·2Me₂CO, 1-RE·2CH₂Cl₂) according to continuous shape measurements (Table S1†) performed with the Shape 2.1 software,[40,41] consistent with previous reports for 1-Yb and related mononuclear [RE(HB(pz)₃)₂L] complexes, where L = tropolonate or benzoate.[36,42] Bond length analysis of the Y(III) analogues shows

Table 1 Crystal data for compounds 1-Y·2Me₂CO, 1-Y·2CH₂Cl₂, 1-Dy·2CH₂Cl₂, 2-Y, 3-Y·1.2CH₂Cl₂, 4-Y·3.5MeOH and 5-Y·5MeOH

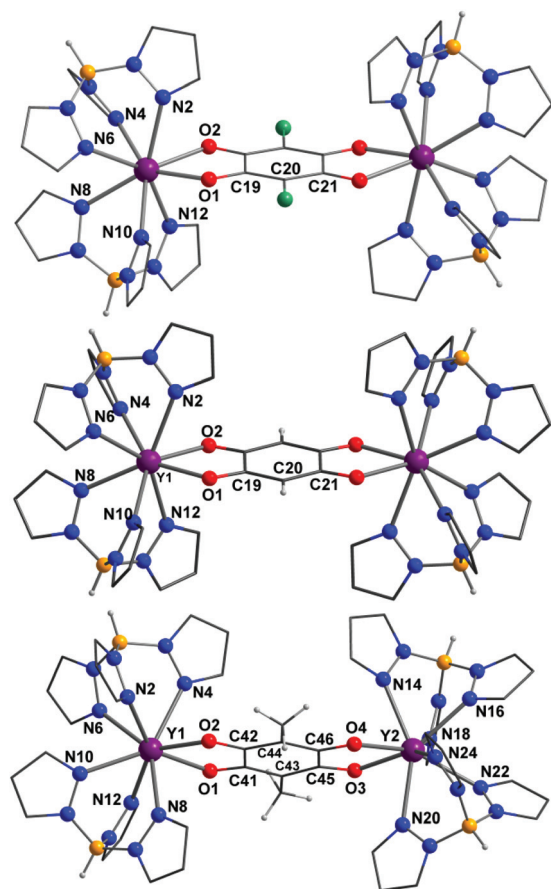|	1-Y·2Me₂CO	1-Y·2CH₂Cl₂	1-Dy·2CH₂Cl₂	2-Y	3-Y·1.2CH₂Cl₂	4-Y·3.5MeOH	5-Y·5MeOH
Empirical formula	C₄₈H₅₂B₂Cl₂N₂₄O₆Y₂	C₄₄H₄₄B₄Cl₆N₂₄O₄Y₂	C₄₄H₄₄B₄Cl₆Dy₂N₂₄O₄	C₄₂H₄₂B₄N₂₄O₄Y₂	C₄₄H₄₆B₄N₂₄O₄Y₂	C₄₀.₅H₇₆B₄N₁₂O₁₈.₅Y₂	C₇₃.₃H₁₃₀.₇B₆Cl₂N₂₄O₃₀Y₄
Formula weight	1353.09	1406.79	1553.97	1168.05	1196.11	1248.19	2320.24
Temperature/K	130.01(10)	100(2)	100(2)	100(2)	100(2)	130.01(10)	130.01(10)
Crystal system	Monoclinic	Monoclinic	Monoclinic	Monoclinic	Trigonal	Triclinic	Monoclinic
Space group	P2₁/n	P2₁/n	P2₁/n	P2₁/n	R3̄	P1̄	P2₁/c
a/Å	14.2804(4)	13.940(3)	13.934(3)	11.590(2)	49.226(7)	10.3026(8)	13.1868(3)
b/Å	15.0832(3)	15.052(3)	15.037(3)	18.380(4)	49.226(7)	11.8817(7)	21.4815(4)
c/Å	14.6373(4)	14.280(3)	14.836(3)	12.150(2)	13.220(3)	13.8646(11)	19.6434(4)
α/°	90	90	90	90	90	71.183(6)	90
β/°	108.072(3)	107.57(3)	107.72(3)	104.12(3)	90	81.824(6)	101.2134(18)
γ/°	90	90	90	90	120	87.703(6)	90
V/Å³	2997.25(13)	2856.4(11)	2961.1(11)	2510.0(9)	27 743(10)	1590.1(2)	5458.21(19)
Z	2	2	2	2	18	1	2
ρcalc/g cm⁻³	1.499	1.636	1.743	1.545	1.289	1.303	1.412
μ/mm⁻¹	3.975	2.369	2.839	2.369	1.931	3.028	3.880
F(000)	1376.0	1416.0	1524.0	1184.0	10 944.0	649.0	2398.0
Radiation	CuKα	Synchrotron	Synchrotron	Synchrotron	Synchrotron	CuKα	CuKα
λ/Å	1.54184	0.71080	0.71080	0.71080	0.71080	1.54184	1.54184
2Θ range/°	7.556 to 154.37	3.578 to 65.698	3.512 to 64.052	4.106 to 63.74	1.654 to 63.708	7.862 to 147.83	6.834 to 155.184
Reflections collected	30 166	55 283	71 573	71 257	260 816	11 043	60 720
Independent reflections	6302	7662	9096	7549	19 276	6215	11 486
Data/restraints/parameters	6302/0/390	7662/0/380	9096/0/380	7549/0/343	19 276/0/705	6215/6/429	11 486/12/688
Rint	0.0508	0.0901	0.0568	0.1528	0.1746	0.0435	0.0731
Goodness-of-fit on F²	1.036	1.049	1.054	1.061	1.035	1.046	1.059
R₁, wR₂ [I ≥ 2σ(I)]	0.0338, 0.0825	0.0454, 0.1156	0.0335, 0.0795	0.0595, 0.1272	0.0576, 0.1335	0.0562, 0.1509	0.0558, 0.1444
R₁, wR₂ [all data]	0.0433, 0.0885	0.0589, 0.1241	0.0473, 0.0846	0.1144, 0.1499	0.1118, 0.1547	0.0639, 0.1622	0.0624, 0.1502
Δρmax,min/e Å⁻³	0.83/−0.55	1.15/−2.03	1.60/−2.03	0.55/−1.70	0.43/−1.67	1.55/−1.18	1.37/−1.46

Fig. 1 Structural representations of the dinuclear complexes in **1-Y**·2Me$_2$CO (top), **2-Y** (middle) and **3-Y**·1.2CH$_2$Cl$_2$ (bottom), pyrazole hydrogen atoms have been omitted for clarity. Colour code: Y (purple), O (red), N (blue), B (orange), Cl (green), C (black), H (grey).

similar Y–O and Y–N bond lengths for all complexes, in the respective ranges 2.3–2.4 and 2.4–2.6 Å, despite small differences in the coordination geometries (Table 2). As is usual for

rare earth analogues, the Dy–O/N bond in **1-Dy** are slightly longer than the equivalent Y–O/N bonds in **1-Y** due to the lanthanoid contraction.

Using a method reported for assigning Δ and Λ stereo-isomers in complexes with coordination numbers greater than six, the absolute configurations in the three families in solid state were investigated, assuming idealised square antiprismatic geometry.[43] The complexes **1-Y** (in both **1-Y**·2Me$_2$CO and **1-Y**·2CH$_2$Cl$_2$) and **2-Y** are present as mesomers, where one Y(III) per molecule has Λ and one has Δ absolute configuration, as expected for dinuclear species where the centroid coincides with an inversion centre. In **3-Y** both Y(III) centres in a given molecule have the same absolute configuration and both Δ, Δ and Λ, Λ enantiomers are present in the crystal lattice in equal amount. Tetraoxolene C–C and C–O bond lengths are all consistent with the dianionic oxidation state assigned, with the ligand adopting a delocalised bis-bidentate binding mode.[44] The intramolecular Y⋯Y distances are also similar for the three families.

The compounds **1-Y**·2Me$_2$CO, **1-Y**·2CH$_2$Cl$_2$ and **1-Dy**·2CH$_2$Cl$_2$ exhibit the same crystal packing, with the solvent molecules occupying equivalent sites in each structure. Crystal packing diagrams for **1-Y**·2Me$_2$CO, **2-Y**, **3-Y**·1.2CH$_2$Cl$_2$ (Fig. S4†) indicate that the only compound to crystallise solvent-free, **2-Y**, exhibits π–π interactions between pyrazole rings of neighbouring molecules. These strong intermolecular interactions likely account for the relative insolubility of the **2-RE** family compared to **1-RE** and **3-RE**.

Compound **4-Y**·3.5MeOH crystallises in the triclinic space group $P\bar{1}$ with half a dinuclear complex per asymmetric unit. The dinuclear structure of neutral **4-Y** (Fig. 2) is related to that of the **3-RE** family, with one HB(pz)$_3$$^-$ ligand per metal centre replaced by a bidentate B(OMe)$_4$$^-$ ligand and the eighth yttrium coordination site occupied by a monodentate MeOH ligand. Compound **5-Y**·5MeOH crystallises in the monoclinic $P2_1/c$ space group with half a tetranuclear complex per asymmetric unit. Complex **5-Y** is related to **4-Y** and can be con-

Table 2 Selected interatomic distances (Å) for **1-Y**·2Me$_2$CO, **1-Y**·2CH$_2$Cl$_2$, **2-Y** and **3-Y**·1.2CH$_2$Cl$_2$

Distance[a]	1-Y·2Me$_2$CO	1-Y·2CH$_2$Cl$_2$	2-Y	3-Y·1.2CH$_2$Cl$_2$	
				Y1	Y2
Y–O$_1$ (O$_3$)	2.342(2)	2.272(2)	2.313(3)	2.2989(2)	2.309(2)
Y–O$_2$ (O$_4$)	2.360(2)	2.345(2)	2.344(3)	2.333(2)	2.298(2)
Y–N$_2$ (N$_{14}$)	2.504(2)	2.519(2)	2.552(3)	2.450(3)	2.539(3)
Y–N$_4$ (N$_{16}$)	2.467(2)	2.451(2)	2.435(3)	2.555(3)	2.486(3)
Y–N$_6$ (N$_{18}$)	2.513(2)	2.382(2)	2.473(3)	2.482(3)	2.459(3)
Y–N$_8$ (N$_{20}$)	2.530(2)	2.447(2)	2.505(3)	2.485(3)	2.511(3)
Y–N$_{10}$ (N$_{22}$)	2.447(2)	2.489(3)	2.472(3)	2.518(3)	2.515(3)
Y–N$_{12}$ (N$_{24}$)	2.424(2)	2.450(2)	2.516(3)	2.464(3)	2.454(3)
C$_{19}$–O	1.258(3)	1.248(3)	1.264(4)	1.270(4) (C$_{41}$–O$_1$)	1.274(4) (C$_{45}$–O$_3$)
C$_{21}$–O$_2$	1.252(3)	1.218(3)	1.267(4)	1.273(4) (C$_{42}$–O$_2$)	1.271(4) (C$_{46}$–O$_4$)
C$_{19}$–C$_{20}$	1.389(3)	1.355(3)	1.396(5)	1.398(4) (C$_{41}$–C$_{43}$)	1.396(4) (C$_{44}$–C$_{46}$)
C$_{20}$–C$_{21}$	1.402(3)	1.390(4)	1.389(5)	1.399(4) (C$_{42}$–C$_{44}$)	1.393(4) (C$_{43}$–C$_{45}$)
C$_{19}$–C$_{21}$	1.539(3)	1.516(4)	1.532(5)	1.526(4) (C$_{41}$–C$_{42}$)	1.528(4) (C$_{45}$–C$_{46}$)
Intramolecular Y⋯Y	8.599(1)	8.420(2)	8.543(1)	8.464(2)	
Intermolecular Y⋯Y[b]	8.700(1)	8.999(1)	7.973(2)	8.254(2)	

[a] In brackets are atom-labelling for Y2 and tetraoxolene in **3-Y**. [b] Shortest distance.
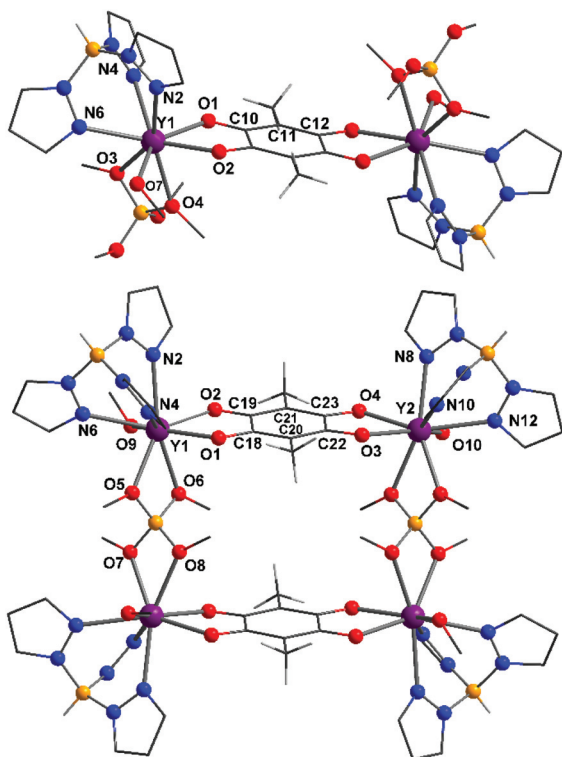
Fig. 2 Structural representations of the yttrium complexes in 4-Y·3.5MeOH (top) and 5-Y·5MeOH (bottom); colour code as per Fig. 1.

sidered to be comprised of two units of 4-Y linked through two bis-bidentate B(OMe)$_4^-$ ligands, although the eighth coordination site on Y2 is occupied by a 70 : 30 disordered terminal MeOH/H$_2$O ligand. The compounds 4-Y and 5-Y both exhibit hydrogen bonding interactions between the methanol solvent molecules and coordinated methanol ligands (Fig. S5†). The tetranuclear complex in 5-Y is overall dicationic, with charge balance provided by chloride counterions. The yttrium coordination geometry is best described as triangular dodecahedral in both 4-Y and 5-Y (Table S1†) and the bond lengths are in the ranges evident for the other complexes (Table S2†). The B(OMe)$_4^-$ ligand has been observed in complexes and coordination polymers previously, binding in the bidentate or bis-bidentate modes observed in 4-Y and 5-Y.[39,45] The structure of complex 5-Y can be described as a supramolecular square or grid, which are much less common for rare earth metals than for transition metals.[46]

Infrared spectroscopy

The infrared spectra of 1-RE·2CH$_2$Cl$_2$, 2-RE and 3-RE·xCH$_2$Cl$_2$ were measured as pressed KBr disks (Fig. S6 and S7†). The spectra of the different rare earth analogues of the three structural families vary little, consistent with the isostructural nature of the complexes. All spectra exhibit strong vibrational modes attributed mostly to stretches associated with the HB(pz)$_3^-$ ligand. A single B–H stretch of the HB(pz)$_3^-$ is seen at ~2450 cm^{-1}, confirming the presence of the coordinated tripodal ligand. Bands attributed to modes involving the tetra-

oxolene ligands include the band at 1540 cm^{-1} in 2-Y which shifts to lower energy with increasing electron donation from the substituents to 1527 cm^{-1} in 3-Y, which is attributed to a ν_{CO} stretch, as well as the bands at 1404 and 1437 cm^{-1}.

Electronic spectroscopy

Diffuse reflectance UV-visible spectra were measured for solid samples of all compounds 1-RE·2CH$_2$Cl$_2$, 2-RE and 3-RE·xCH$_2$Cl$_2$ dispersed in KBr, while solution absorbance spectra were also acquired for the soluble 1-RE and 3-RE in acetonitrile, as well as for the deprotonated tetraoxolene ligands (Fig. S8–S10†). The solution spectra for 1-RE and 3-RE remain unchanged over at least 24 hours, consistent with stability of the complexes in acetonitrile and the solution and solid state spectra are in good agreement. The three major bands in the diffuse reflectance spectra of 1-RE, 2-RE and 3-RE are attributed to ligand-centred π–π* transitions for the bands at ~220 nm and ~350 nm and to a ligand-centred n–π* transition for the broad band with a low extinction coefficient over the visible range (Fig. S9†). The bands are assigned to transitions based on the tetraoxolene ligands by comparison with the solution spectra of the deprotonated tetraoxolene ligands, as well as similar literature complexes.[36,47]

The spectra for the different members of the 1-RE, 2-RE, and 3-RE families with different rare earth metals are very similar (Fig. S9†), with little variation with the metal. There are no obvious charge-transfer bands involving the rare earth metal and redox-active tetraoxolene ligand.[48] For the three Ho^{3+} analogues, additional sharp bands corresponding to f–f transitions in the Ho^{3+} ion are evident in the diffuse reflectance spectra (Fig. S10†). The three features that are observed are assigned as $^5I_8 \rightarrow {}^5G_5$ (418 nm), $^5I_8 \rightarrow {}^5G_6$, $^5F_1$ (452 nm) and $^5I_8 \rightarrow {}^5F_4$ (538 nm) transitions.[49]

Electrochemistry

Following confirmation of solution stability of 1-RE and 3-RE by electronic absorption and ^{1}H NMR spectroscopy (for the Y analogues), the voltammetric behaviour of acetonitrile solutions of 1-RE (RE = Y, Eu, Tb, Dy, Yb) and 3-Y with 0.1 M Bu$_4$NPF$_6$ as the supporting electrolyte were examined using a glassy carbon working electrode (Fig. 3 and S11†). The measured oxidation (E_{pa}) and reduction (E_{pc}) peak potentials (E_p) from the cyclic voltammograms (100 mV s^{-1} scan rate) are tabulated in Table 3, together with the mid-point potentials (E_m) and peak-to-peak separations (ΔE_p) for the quasi-reversible processes. All potentials are quoted versus the ferrocene/ferrocenium (Fc/Fc$^+$) couple.

The 1-RE complexes measured all exhibit two reductions (processes I and II) and an oxidation (process III) at similar potentials (Table 3, Fig. 3 and S11†), which are all assigned as tetraoxolene ligand-based processes (Scheme 1), consistent with similar literature complexes.[47] For both reductions I and II in 1-Y, the E_m values are independent of scan rate at −0.90 V and −1.73 V, respectively. The current ratios i_{pc}/i_{pa} for both processes are close to unity, where i_{pa} and i_{pc} are the peak anodic and peak cathodic currents respectively. A plot of the
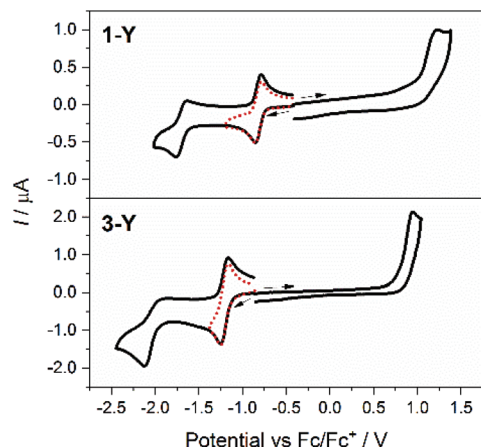
Fig. 3 Cyclic voltammograms of **1-Y** and **3-Y** (0.5 or 1.0 mM in MeCN, respectively, with 0.1 M Bu$_4$NPF$_6$) obtained with a 1 mm diameter glassy carbon working electrode at a scan rate of 100 mV s^{-1}. The dashed red lines plot the voltammograms measured with a switching potential immediately past the first reduction to probe reversibility. The anodic and cathodic regions were scanned separately as indicated by the arrows.

Table 3 E_p or E_m/V (ΔE_p/mV) for **1-RE** and **3-Y**

	E_p or E_m/V (ΔE_p/mV)		
	Reduction (E_m)		Oxidation (E_{pa})
Compound	I	II	III[a]
1-Y	−0.96 (75)	−1.73 (90)	1.18
1-Eu	−0.815 (80)	−1.65 (180)	1.17
1-Tb	−0.813 (80)	−1.66 (105)	1.13
1-Dy	−0.828 (75)	−1.69 (90)	1.11
1-Yb	−0.847 (75)	−1.68 (120)	0.67
3-Y	−1.21 (75)	−2.11[a]	0.89

[a] E_{pc} or E_{pa} at a scan rate of 100 mV s^{-1}.
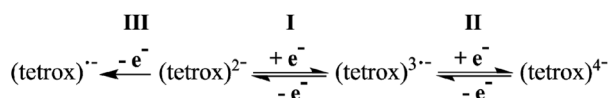
Scheme 1 Electrochemical processes (I, II and III) for **1-RE** (RE = Y, Eu, Tb, Dy and Yb) and **3-Y**.

cathodic peak current *versus* the square root of the scan rate is linear for process **I** only, following the Randles–Sevcik model for reversible systems.[50] For an ideal reversible one-electron process, ΔE_p should be 59 mV and for process **I** the ΔE_p of 75 mV at a scan rate of 100 mV s^{-1} is the same as that measured for the Fc/Fc$^+$ couple under these conditions, consistent with the assignment of **I** as a diffusion controlled and reversible one-electron process. Process **II** has a ΔE_p of 95 mV and the plot of the cathodic peak current *versus* the square

root of the scan rate is non-linear, consistent with assignment of process **II** as quasi-reversible. The oxidation process **III** shows no current response on the reverse sweep and is clearly irreversible. It is tentatively assigned to a one-electron oxidation to the monoanionic form of the tetraoxolene ligand, although steady-state voltammetry or coulometry would be required to confirm this assignment.

The voltammograms measured for the other analogues of **1-RE** are very similar to that for **1-Y**, with no additional metal-centred redox processes observed for the commonly redox-active Eu(III), Tb(III) and Yb(III) ions; however, the potentials of the lanthanoid complexes are shifted around 100 mV more positive than for **1-Y**. The complexes **1-Eu** and **1-Yb** seem to be less stable in solution than the other **1-RE** complexes, and the reductive processes exhibit decreased reversibility than the other analogues (Fig. S11†).

The voltammograms measured for **3-Y** are qualitatively similar to those for **1-Y** (Fig. 3, Table 3; Scheme 1), with all processes shifted more negative by around 200–300 mV. This is consistent with the electron donating/withdrawing characteristics of the substituents on the bridging tetraoxolene ligands and the more difficult reduction of the Me$_2$dhbq^{2-} ligand *versus* the ca^{2-} analogue. The cyclic voltammogram of **3-Y** shows one diffusion-controlled reversible reduction at E_m = −1.22 V (**I**), which fulfils the same requirements of reversibility as those of the first reduction process in **1-Y**. The second reduction process (**II**) for **3-Y** at E_{pc} = −2.11 V exhibits a smaller anodic current on the reverse sweep than the equivalent process in **1-Y**, consistent with less chemical reversibility or slower electron transfer kinetics.

Efforts to access a radical-bridged analogue

The ultimate target of this work at the outset was an analogue of compounds **1-RE**, **2-RE** or **3-RE** that incorporates the bridging tetraxolene in a radical oxidation state, to explore the SMM properties. From the voltammetric studies the most promising approach would appear to be through one-electron reduction of the **1-RE** family to access the tetraoxolene in the radical trianionic form, as the first reduction potential (process **I**) is more positive for the **1-RE** family than for the **3-RE** family and the **2-RE** family is insoluble. Oxidation to a radical monoanionic form might also be possible, although the irreversibility of the first oxidation process (**III**) in the voltammetry of **1-RE** and **3-RE** suggests that the oxidised form might be unstable. To our knowledge the radical monoanionic redox state of the ligand has never been reported in a metal complex. We attempted reduction of **1-RE** (RE = Y, Gd, Tb and Dy) using one equivalent of cobaltocene in rigorously anaerobic and anhydrous conditions. An immediate colour change from purple to green occurred, suggesting that the desired reaction had proceeded. However, the reduced compounds are unstable and all our efforts to isolate and purify the target radical-bridged dinuclear complex have been unsuccessful so far, with efforts to recrystallise the obtained solid instead affording crystals of a mononuclear decomposition product.

Static magnetic properties and EPR spectroscopy

Magnetic susceptibility data were acquired for analytically pure bulk samples of the easier to purify Me$_2$dbhq^{2-} compounds **3-Gd**·2CH$_2$Cl$_2$, **3-Tb**·0.7CH$_2$Cl$_2$ and **3-Dy**·1.1CH$_2$Cl$_2$ as well as the ca^{2-} analogue **1-Dy**·2CH$_2$Cl$_2$. The Tb(III) and Dy(III) complexes were of interest due to their potential SMM behaviour and the Gd(III) analogue provides a useful spin-only comparison for evaluation of any exchange interaction. The magnetic properties of the other **1-RE** and **3-RE** analogues were not measured and bulk samples of **2-RE** of sufficient purity for magnetic analysis could not be obtained. Variable temperature magnetic susceptibility measurements are shown in Fig. 4 and magnetisation *versus* field data are available in Fig. S12 and S13.† The room temperature $\chi_M T$ values are 15.2, 22.3, 27.2 and 28.8 cm^3 mol^{-1} K, for **3-Gd**·2CH$_2$Cl$_2$, **3-Tb**·0.7CH$_2$Cl$_2$, **3-Dy**·1.1CH$_2$Cl$_2$, and **1-Dy**·2CH$_2$Cl$_2$, respectively. All these values are within 5% of the values expected for two non-interacting free lanthanoid(III) ions (Gd(III), $^8S_{7/2}$: 15.8 cm^3 mol^{-1} K; Tb(III), $^7F_6$: 23.6 cm^3 mol^{-1} K; Dy(III), $^6H_{15/2}$: 28.3 cm^3 mol^{-1} K).

The thermal behaviour of the Gd(III) derivative – for which the CF effects do not mask the exchange ones due to the absence of orbital degeneracy – clearly indicates that the two Gd(III) centres are non-interacting: the $\chi_M T$ value is constant throughout the investigated temperature range, following Curie–Weiss behaviour (Fig. S14†) with respective Curie and Weiss constants of C = 15.2 cm^{-3} mol K^{-1} and θ = 0.15 K. The powder X-band ($\nu \sim$ 9.4 GHz) EPR spectrum measured at 10 K (Fig. S15†) confirms this interpretation. Preliminary analysis of the EPR spectrum on the basis of the spin Hamiltonian:

$$\hat{H} = D\hat{S}_z^2 + E(\hat{S}_x^2 - \hat{S}_y^2) + g\beta\mathbf{S}\cdot\mathbf{H} \tag{1}$$

where D and E are the axial and rhombic zero-field splitting parameters, respectively, indicates 0.1 cm^{-1} < $|D|$ < 0.15 cm^{-1} and $E/D \sim$ 0.1,[51] which is in the same order of magnitude previously reported for related [Gd(HB(pz)$_3$)$_2$(L)] (L = tropolonate and 3,5-di-*tert*-butyl-seminquinonate) complexes.[52] This picture is further confirmed by the measured isothermal field-dependent magnetisation curves (Fig. S13†), which are consistent with two non-interacting S = 7/2 spins with a small zero
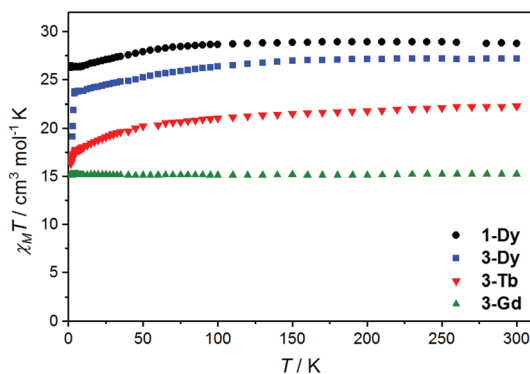
field splitting. These data were fit using the computer program PHI,[53] constraining E = 0 to reduce overparameterisation, providing the following best fit parameters: $|D|$ = 0.09 ± 0.02 cm^{-1}, which is very close to the value estimated from EPR, and g = 1.94 ± 0.01. The somewhat low g value compared to the expected value of 1.99 probably reflects a 2–3% error in sample weighing and can be regarded as physically irrelevant.[54]

Having established the absence of a measurable exchange interaction for **3-Gd**·2CH$_2$Cl$_2$, the temperature dependence of $\chi_M T$ observed for the derivatives containing anisotropic lanthanoid ions can be unequivocally attributed to the progressive depopulation, upon decreasing temperature, of the excited levels arising from the CF splitting of the ground J multiplets of Dy(III) and Tb(III). In the case of **1-Dy** and **3-Dy** this results in relatively well isolated ground doublets, as witnessed by the saturation of M *vs.* H curves measured at low temperature (Fig. S12†). The non-Kramers nature of the Tb(III) ion, on the other hand, affords some non-negligible field induced inter-action among the lowest lying levels, which is evident from the linear increase of the magnetisation *versus* field curves at higher field.

No EPR spectrum was observed for the two Dy(III) derivatives, possibly due to fast relaxation or a low intra-doublet transition probability because of the ground-state composition. A broad, uninformative band at zero field, quite common for Tb(III) molecular systems,[55] is evident for **3-Tb** (Fig. S15†).

Dynamic magnetic properties

Alternating current (ac) magnetic susceptibility data were measured for **3-Tb**·0.7CH$_2$Cl$_2$, **3-Dy**·1.1CH$_2$Cl$_2$ and **1-Dy**·2CH$_2$Cl$_2$ to probe for SMM behaviour in the temperature range 2–14 K and frequency (ν) range 1–10 000 Hz. No frequency-dependence of the magnetic susceptibility was observed for **3-Tb**·0.7CH$_2$Cl$_2$ either without an applied dc field or with a field up to 3 kOe, which is likely due to fast QTM or the lack of a doubly degenerate ground state for this non-Kramers ion, given the relatively low symmetry crystal field. In contrast, the two Dy(III) derivatives exhibit rich dynamic behaviour, which is both field- and temperature-dependent. At low temperature and zero applied dc field, a relatively fast process is evident, occurring at ν > 10 000 Hz for **1-Dy**·2CH$_2$Cl$_2$ at 4 K and at $\nu \sim$ 1000 Hz for **3-Dy**·1.1CH$_2$Cl$_2$ at 2 K (Fig. S16†). For **1-Dy**·2CH$_2$Cl$_2$, the zero-field relaxation was simply too fast to characterise the behaviour in the range of frequencies available on our instrument. However, variable temperature measurements for slower-relaxing **3-Dy**·1.1CH$_2$Cl$_2$ (Fig. 5 left) clearly show a temperature-independent peak in χ''_M in the temperature range 1.9–4.5 K due to QTM, which is also apparent from the Arrhenius plot of the temperature dependence of the relaxation times (Fig. S17†).

For both derivatives, the fast relaxation channel is suppressed by the application of a dc field (Fig. 5 centre and right), which triggers the onset of a much slower process, reaching the slowest rate for **1-Dy**·2CH$_2$Cl$_2$ upon application of a 1.6 kOe dc field (Fig. S16†). This behaviour is quite common

Fig. 4 Plot of $\chi_M T$ *versus* T for **1-Dy**·2CH$_2$Cl$_2$, **3-Gd**·2CH$_2$Cl$_2$, **3-Dy**·1.1CH$_2$Cl$_2$ and **3-Tb**·0.7CH$_2$Cl$_2$.
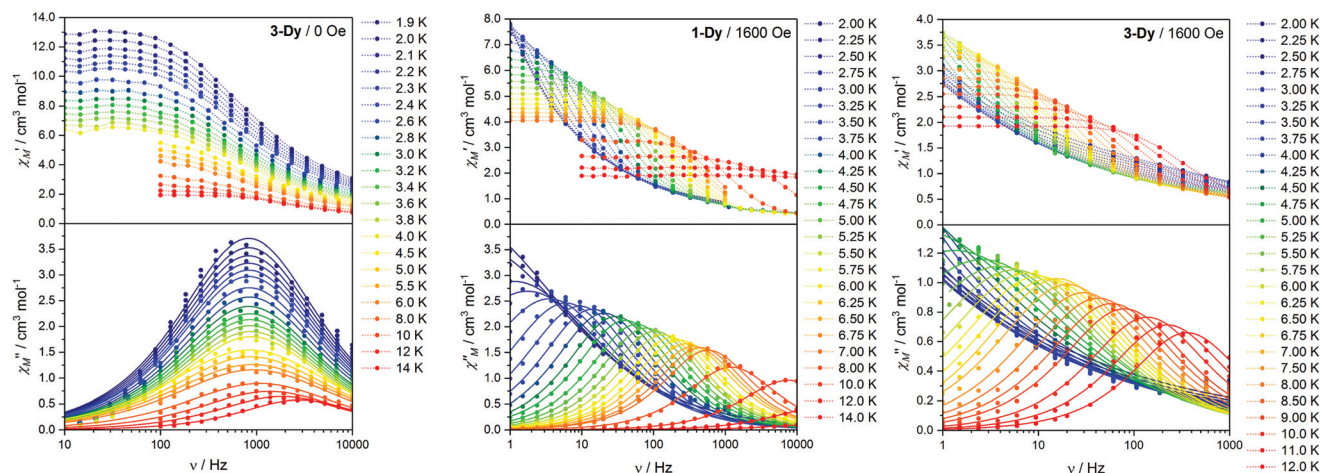
Fig. 5 Temperature dependence of the in-phase (top) and out-of-phase (bottom) ac magnetic susceptibility as a function of frequency (ν) for: (left) **3-Dy**·1.1CH$_2$Cl$_2$ with zero applied dc field, (centre) **1-Dy**·2CH$_2$Cl$_2$ with a 1.6 kOe dc field, and (right) **3-Dy**·1.1CH$_2$Cl$_2$ with a 1.6 kOe dc field. The solid lines represent the fits of χ''_M to the Debye equation as described in the text.

in lanthanoid-based SMMs and can be attributed to the competing effects of two different relaxation processes: the faster one, dominant in zero field, is directly related to relaxation of the magnetisation *via* QTM, induced by dipolar and hyperfine interactions; the slower process is linked to thermally-activated relaxation (direct, Raman or Orbach).[20,56–58] Since determination of the optimum dc field was not possible for **3-Dy**·1.1CH$_2$Cl$_2$, as the in-field relaxation is too slow at low temperature, we performed the study of the temperature dependence of the relaxation rate of the magnetisation for both complexes with an applied field of 1.6 kOe. Quantitative determination of the relaxation time τ was obtained by fitting the χ''_M *versus* ν curves with the generalised Debye equation,[59] and the corresponding temperature dependences are shown as Arrhenius plots for the two compounds (Fig. 6). It is evident that while the relaxation of **3-Dy**·1.1CH$_2$Cl$_2$ is linear, this is not the case for **1-Dy**·2CH$_2$Cl$_2$. Accordingly, data for

3-Dy·1.1CH$_2$Cl$_2$ could be fit by assuming a simple Orbach process with $\tau_0 = 1.0 \times 10^{-5}$ s and $U_{eff} = 47$ K, while a fit of the temperature dependence of **1-Dy**·2CH$_2$Cl$_2$ required testing with different combinations of relaxation processes according to:[14]

$$\tau^{-1} = \tau_{QTM}^{-1} + \tau_0^{-1} \exp(U_{eff}/k_B T) + CT^n + AT \qquad (2)$$

where the first term represents the rate of QTM, the second is the rate of the Orbach process, the third is the Raman process (parameterised by C and n) and the fourth term is the rate of the direct process (parameterised by A). The best fit was obtained by assuming $\tau_0 = 3 \times 10^{-5}$ s, $U_{eff} = 24$ K, $C = 2.7 \times 10^{-3}$ s K^{-n} and fixing $n = 7$. No reasonable fit could be obtained by including either QTM and/or direct relaxation, possibly because these are minimised at the "optimum" dc field employed. We note that while the value of the Raman exponent n is as expected for the Kramers Dy(III) ions, for both derivatives τ_0 is at the higher end of expected values. This suggests that the obtained parameters should be considered as purely phenomenological, in the absence of further theoretical and/or experimental investigations to confirm the presence of a real state at the 47/24 K necessary to promote Orbach relaxation.[60–62] Ideally a quantitative study of the mechanisms involved in the magnetic relaxation would require investigation of the samples diluted with a diamagnetic rare earth ion, which is beyond the scope of the present study.[63]
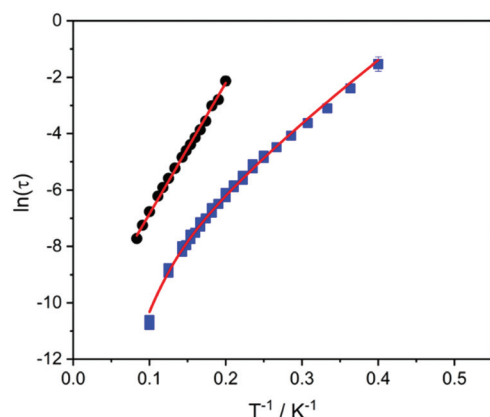
Conclusions

Variation of the substituents on the 3- and 6- positions of the bridging tetraoxolene ligand has afforded three families of neutral dinuclear rare earth complexes with hydrotris(pyrazolyl)borate blocking ligands. Two structurally interesting byproducts that also feature bridging tetraoxolene ligands were also obtained, following partial decomposition of the hydrotris(pyrazolyl)borate ligands in methanol to afford tetramethoxyborate

Fig. 6 Arrhenius plots of relaxation rates of **1-Dy**·2CH$_2$Cl$_2$ (squares) and **3-Dy**·1.1CH$_2$Cl$_2$ (circles) in a 1.6 kOe dc magnetic field with fits (lines) as described in the text.

ligands. For all complexes, the tetraoxolene ligands are in the diamagnetic dianionic form. Solution electrochemical studies of dinuclear complexes confirm the redox-activity of the tetraoxolene ligands, with the electrochemical reversibility of a tetraoxolene-based one-electron reduction suggesting the possibility of accessing an analogue with a trianionic radical bridge following chemical reduction. However, isolation of the one-electron reduced analogue has proved elusive to date.

Magnetochemical and EPR characterisation of one of the dinuclear Gd complexes indicate negligible magnetic coupling between the two Gd(III) ions, either as exchange coupling through the diamagnetic tetraoxolene bridging ligand, or from through-space dipolar coupling. Two Dy(III) analogues both exhibit slow magnetic relaxation, with QTM dominant during ac magnetic susceptibility measurements performed in the absence of an applied dc field. The application of a dc field effectively suppresses the QTM and relaxation data are consistent with an Orbach mechanism playing a major role in relaxation for both compounds. The effective energy barriers to magnetisation reversal are determined as 47 and 24 K for the analogues with the dichloro- and dimethyl-substituted tetraoxolene ligands, respectively. The molecular structures for the two Dy(III) complexes are similar, but the local Dy(III) coordination environments are distinctly different, dodecahedral for **1-Dy**·$2CH_2Cl_2$ and square antiprismatic for **3-Dy**·$1.1CH_2Cl_2$. These structural differences are reflected in the different dynamic magnetic behaviour measured for the two compounds, highlighting once again the number of subtle parameters which might influence the electronic structure and resulting low temperature magnetisation dynamics in lanthanoid complexes.

That slow magnetic relaxation is evident in the present Dy(III) complexes, accompanied by significant zero-field QTM, is promising for future radical-bridged analogues, in which the zero-field QTM may be suppressed by metal–ligand exchange. Regardless of whether the exchange coupling between the Dy(III) ion and the radical ligand is ferro- or antiferromagnetic, radical-bridged dinuclear complexes could well exhibit enhanced SMM properties. Ongoing work in our lab is focused on fine-tuning the chemical properties of the bridging and blocking ligands to facilitate access to related radical-bridged dinuclear lanthanoid(III) complexes.

Experimental

Synthesis

All manipulations were performed under aerobic conditions and all chemicals purchased were of reagent grade or higher and used as received. The Me_2dhbqH_2 and $KHB(pz)_3$ proligands were prepared according to literature procedures.[64,65]

[((HB(pz)₃)₂Y)₂(μ-ca)] (1-Y). A modified literature procedure was followed.[66] A suspension of $KHB(pz)_3$ (97.1 mg, 0.385 mmol) in CH_2Cl_2/EtOH (6 mL) was added to a solution of $Y(NO_3)_3$·$6H_2O$ (73.5 mg, 0.192 mmol) in EtOH (1 mL),

CH_2Cl_2 (10 mL) and the resultant colourless suspension stirred for 10 minutes. A red-purple solution of ca^{2-} was prepared from addition of Et_3N (26.8 μL, 0.192 mmol) to caH_2 (19.8 mg, 0.095 mmol) in CH_2Cl_2 (10 mL). The deprotonated ligand was added dropwise to the solution of $Y(HB(pz)_3)_2(NO_3)$ resulting in a deep violet solution with some fine precipitate, which was removed by filtration. The solution volume was decreased, and a microcrystalline powder collected. The product was recrystallized from a CH_2Cl_2/n-hexane mixture and then vacuum-filtered, washed with n-hexane and air-dried, yielding purple microcrystals of **1-Y**·$2CH_2Cl_2$ (53 mg, 39%). Purple plates of **1-Y** suitable for X-ray diffraction were also obtained from slow evaporation of a solution of **1-Y** in acetone/n-hexane, maintained in contact with mother liquor to prevent desolvation and identified crystallographically as **1-Y**·$2Me_2CO$. ^1H NMR (400 MHz, $CDCl_3$) δ, ppm: 6.00 (t, 12H), 7.01 (d, 12H), 7.65 (d, 12H). UV-visible (MeCN) λ_{max}, nm (ε_M, M^{-1} cm^{-1}): 231 (sh), 277 (4.5×10^3), 337 (2.9×10^4), 349 (3.1×10^4), 556 (1.7×10^2). IR (KBr disk, cm^{-1}): 2850 (w); ν_{BH} 2460 (m, BH), 1533 (s, CO), 1504 (m), 1406 (m), 1388 (m), 1301 (m), 1216 (m), 1201 (w), 1122 (m), 1068 (w), 1051 (m), 978 (m), 851 (w), 780 (w), 760 (m), 723 (m), 670 (w), 620 (w), 460 (w).

[((HB(pz)₃)₂RE)₂μ-ca] (1-Eu, 1-Gd, 1-Tb, 1-Dy, 1-Ho, 1-Er, 1-Yb). The **1-RE** series was synthesised as per **1-Y**, replacing $Y(NO_3)_3$·$6H_2O$ with the corresponding rare earth nitrate. Yields: **1-Eu** (38%), **1-Gd** (39%), **1-Tb** (28%), **1-Dy** (39%), **1-Ho** (50%), **1-Er** (27%), **1-Yb** (20%) of purple microcrystals. Anal. calcd for **1-Dy**·$2CH_2Cl_2$; $Dy_2C_{44}H_{44}N_{24}B_4Cl_6O_4$: C, 34.01; H, 2.85; N, 21.63. Found: C, 34.09; H, 2.84; N, 21.48.

[((HB(pz)₃)₂Y)₂(μ-dhbq)] (2-Y). A suspension of $KHB(pz)_3$ (98.9 mg, 0.392 mmol) in CH_2Cl_2/EtOH (6 mL) was added to a solution of $Y(NO_3)_3$·$6H_2O$ (75.5 g, 0.197 mmol) in CH_2Cl_2 (10 mL) and EtOH (1 mL) and the resultant colourless suspension stirred for 10 minutes. A red solution of $dhbq^{2-}$ was prepared from addition of Et_3N (26.8 μL, 0.192 mmol) to $dhbqH_2$ (13.4 mg, 0.095 mmol) in CH_2Cl_2 (10 mL). The deprotonated ligand was added dropwise to the solution of $Y(HB(pz)_3)_2(NO_3)$ resulting in an intense pink solution with some fine precipitate. The solution was filtered over a Celite plug and left to evaporate. The resultant solid was collected, washed with ether, and air-dried, yielding a pink microcrystalline powder (67 mg, 58%). A crystal suitable for X-ray diffraction was obtained from the reaction solution. UV-visible (reflectance, in ~5% KBr): λ_{max}, nm: 222, 330, 510. IR (KBr disk, cm^{-1}): 2950 (w, CH), 2853 (w), 2452 (w, BH), 1539 (s, CO), 1504 (m), 1404 (m), 1300 (m), 1265 (w), 1215 (m), 1200 (w), 1121 (m), 1049 (m), 978 (w), 819 (w), 760 (m), 723 (w), 673 (s), 621 (w), 457 (w).

[((HB(pz)₃)₂RE)₂(μ-dhbq)] (2-Eu, 2-Gd, 2-Tb, 2-Dy, 2-Ho, 2-Er, 2-Yb). The **2-RE** series was synthesised as per **2-Y**, replacing $Y(NO_3)_3$·$6H_2O$ with the corresponding rare earth nitrate. Yields: **2-Eu** (69%), **2-Gd** (68%), **2-Tb** (64%), **2-Dy** (76%), **2-Ho** (71%), **2-Er** (71%), **2-Yb** (64%) of bright pink microcrystalline powders. Compounds **2-RE** are insoluble in all solvents and recrystallisation was not possible.

[((HB(pz)₃)₂Y)₂(μ-Me₂dhbq)] (3-Y). A suspension of $KHB(pz)_3$ (99.4 mg, 0.394 mmol) in CH_2Cl_2/EtOH (6 mL) was

added to a solution of $Y(NO_3)_3 \cdot 6H_2O$ (75.9 mg, 0.198 mmol) in EtOH (1 mL) and CH_2Cl_2 (10 mL) and the resultant fine colourless suspension stirred for 10 minutes. A dark purple solution of Me_2dhbq^{2-} was prepared from addition of Et_3N (26.8 μL, 0.192 mmol) to Me_2dhbqH_2 (16.3 mg, 0.096 mmol) in CH_2Cl_2 (10 mL). The deprotonated ligand was added dropwise to the rare earth solution resulting in a deep blue-purple solution with some fine precipitate. The solution was filtered over a Celite plug and left to evaporate. The resultant microcrystalline powder was collected and recrystallised from a $CH_2Cl_2/$ n-hexane mixture, and air-dried, yielding purple microcrystals (51 mg, 43%). Thin purple needle-like crystals suitable for X-ray diffraction were obtained from slow evaporation of a $CH_2Cl_2/$n-hexane solution over a few days, maintained in contact with mother liquor to prevent desolvation and identified crystallographically as **3-Y**·$1.2CH_2Cl_2$. ^{1}H NMR (400 MHz, CDCl$_3$) δ, ppm: 1.73 (s, 6H), 5.98 (t, 12H), 6.98 (d, 12H), 7.64 (d, 12H). UV-visible (MeCN) λ_{max}, nm (ε_M, M^{-1} cm^{-1}): 331 (3.4×10^4), 344 (3.4×10^4), 553 (3.1×10^2). IR (KBr disk, cm^{-1}): 2924 (w, CH), 2854 (w); 2462 (w, BH), 1521 (s, CO), 1503 (s), 1403 (m), 1386 (s), 1299 (s), 1214 (m), 1198 (m), 1121 (m), 1051 (s), 977 (w), 778 (w), 763 (m), 723 (m), 671 (w), 621 (w), 460 (w).

[((HB(pz)$_3$)$_2$RE)$_2$(μ-Me$_2$dhbq)] (3-Eu, 3-Gd, 3-Tb, 3-Dy, 3-Ho, 3-Er, 3-Yb). The **3-RE** series was synthesised as per **3-Y**, replacing $Y(NO_3)_3 \cdot 6H_2O$ with the corresponding rare earth nitrate. Crystals obtained have the same needle morphology. Yields: **3-Eu** (38%), **3-Gd** (44%), **3-Tb** (36%), **3-Dy** (45%), **3-Ho** (45%), **3-Er** (33%), **3-Yb** (27%) of purple microcrystals. The degree of solvation of the bulk samples differs slightly for the different metals, as indicated by elemental and thermogravimetric analysis. Anal. calcd for **3-Gd**·$2CH_2Cl_2$; ($Gd_2C_{46}H_{50}N_{24}B_4Cl_4O_4$): C, 36.77; H, 3.35; N, 22.37. Found: C, 36.95; H, 3.09; N, 21.75. Anal. calcd for **3-Tb**·$0.7CH_2Cl_2$; $Tb_2C_{44.7}H_{47.4}N_{24}B_4Cl_{1.4}O_4$: C, 38.47; H, 3.42; N, 24.09. Found: C, 38.93; H, 3.65; N, 23.60. Anal. calcd for **3-Dy**·$1.1CH_2Cl_2$; $Dy_2C_{47.1}H_{52.2}N_{24}B_4Cl_{1.1}O_4$: C, 37.70; H, 3.38; N, 23.40. Found: C, 38.17; H, 3.56; N, 22.89.

[((HB(pz)$_3$)(MeOH)(B(OMe)$_4$)Y)$_2$(μ-Me$_2$dhbq)] (4-Y). A suspension of $KHB(pz)_3$ (48.9 mg, 0.194 mmol) in MeOH (3 mL) was added to a solution of $YCl_3 \cdot 6H_2O$ (30.0 mg, 0.099 mmol) in MeOH (3 mL) and the resultant solution refluxed for 30 minutes with stirring. A solution of Me_2dhbqH_2 (8.0 mg, 0.047 mmol) deprotonated with Et_3N (13.4 μL, 0.096 mmol) in MeOH (5 mL) was added dropwise. The solution was allowed to crystallise at 4 °C for a week, yielding purple rhombohedral plates that were manually separated for structural analysis. It was not possible to obtain a pure bulk sample.

[{((HB(pz)$_3$)(MeOH)$_{0.85}$(H$_2$O)$_{0.15}$Y)$_2$(μ-B(OMe)$_4$)}$_2$(μ-Me$_2$dhbq)$_2$]Cl$_2$ (5-Y). A suspension of $KHB(pz)_3$ (48.9 mg, 0.194 mmol) in MeOH (3 mL) was added to a solution of $YCl_3 \cdot 6H_2O$ (30.5 mg, 0.101 mmol) in MeOH (3 mL) and refluxed for 30 minutes with stirring. A solution of Me_2dhbqH_2 (8.3 mg, 0.049 mmol) deprotonated with Et_3N (13.4 μL, 0.096 mmol) in MeOH (5 mL) was added dropwise. The solution was allowed to crystallise at −18 °C, yielding small purple plates that were manually separated for structural analysis. It was not possible to obtain a pure bulk sample.

X-ray diffraction and structure solution

The crystallographic data (Table 1) for **1-Y**·$2Me_2CO$, **4-Y**·$3.5MeOH$, and **5-Y**·$5MeOH$, were collected at 130 K using an Agilent Technologies SuperNova Dual Wavelength single crystal X-ray diffractometer using Cu-Kα radiation (λ = 1.5418 Å) fitted with a mirror monochromator. Data reduction was performed using CrysAlisPro software (Version 1.171.38.41) using a numerical absorption correction based on Gaussian integration over a multifaceted crystal model. Data for **1-RE**·CH_2Cl_2, **2-Y**, and **3-Y**·$1.2CH_2Cl_2$ were collected at the MX1 beamline at the Australian Synchrotron, tuned to approximate Mo-Kα radiation (λ = 0.7108 Å) fitted with a silicon double crystal monochromator, as crystals of these three compounds were small and poorly diffracting. Data reduction was performed with XDS,[67] using strong multi-scan absorption correction in SADABS.[68] Where necessary, for crystals in monoclinic space groups, multiple runs were collected at different angles and merged with SADABS. Crystals of **1-RE**·CH_2Cl_2 suffered radiation damage and these structures consequently have low completeness of the data.

Crystals were transferred directly from mother liquor to oil to prevent solvent loss. The structures were solved using the intrinsic phasing routine in SHELXT and refined using a full-matrix least squares procedure based on F^2 using SHELXL.[69,70] The positions of all non-hydrogen atoms were refined using anisotropic displacement factors. Hydrogen atoms were placed geometrically and their positions were constrained to geometrical estimates during the refinement, using the riding model. The structure of **3-Y** revealed the presence of highly disordered solvent dichloromethane which proved difficult to model, accordingly refinement was continued using the solvent mask routine in Olex2, with the number of solvent molecules assigned on the basis of the residual electron density and void volume; the final composition of this compound was **3-Y**·$1.2CH_2Cl_2$. For **4-Y**·$3.5MeOH$ and **5-Y**·$5MeOH$, the methanol solvent was partially disordered. As well, for **5-Y**·$5MeOH$, the chloride anion was disordered, and the coordinated solvent molecule was found to be disordered methanol and water. For both compounds, it was possible to model this disorder, using appropriate constraints and restraints, by treating the molecules as being disordered over two or three components.

X-ray powder diffraction data were measured on the Agilent Technologies SuperNova Dual Wavelength single crystal X-ray diffractometer using Cu-Kα radiation at 130 K. Powder samples were prepared by crushing the samples gently and were loaded in a glass capillary for measurement. Data were collected to $2\theta = 70°$ with an exposure time of 60 s per frame.

Spectroscopic measurements

Solution-state electronic absorption spectra were measured on an Agilent Technology Cary 60 UV-visible spectrometer. Diffuse reflectance UV-visible spectra were measured on samples diluted ~5% in KBr on a Thermo Scientific Evolution 220 UV-visible spectrophotometer. Fourier transform infrared spectra were

measured as KBr disc on a Bruker Tensor 27 FTIR spectrometer and normalised as absorbance spectra. X-band (ν = 9.41 GHz) spectroscopic studies on the microcrystalline powder samples were carried out at low temperatures using a Bruker E500 spectrometer equipped with an ESR900 (Oxford Instruments) continuous-flow ^{4}He cryostat. All ^{1}H NMR spectra were acquired on a Varian MR400 400 MHz spectrometer and referenced to residual protic solvent.

Magnetic measurements

All magnetic measurements were performed on powder samples pressed into pellets with PTFE tape to avoid preferential orientation of crystallites induced by magnetic torque. The dc susceptibility and magnetisation measurements were performed on a Quantum Design SQUID magnetometer, with dc susceptibility measurements measured between 1.8 and 300 K. Measurements were corrected for the diamagnetic contribution of the PTFE tape. The ac susceptibility measurements were measured on a Quantum Design PPMS magnetometer equipped with the ac measurement system (ACMS) option.

Electrochemical measurements

Cyclic voltammetry was performed using a standard three-electrode cell configuration under a N_2 atmosphere, using a 3 mm diameter glassy-carbon working electrode, a Pt-wire auxiliary electrode and a leak-free Ag/AgCl reference electrode calibrated against the ferrocene/ferrocenium (Fc/Fc$^+$) couple. All electrochemical measurements were undertaken with 1 or 0.5 mM analyte in MeCN with 0.1 M Bu$_4$NPF$_6$ as the supporting electrolyte.

Other measurements

Elemental analyses (CHN) were performed at the Campbell Microanalytical Laboratory, University of Otago. Thermogravimetric analyses were performed on a Mettler Toledo thermal analyser using a ramp rate of 5 °C per minute up to a maximum temperature of 400 °C and a N_2 atmosphere.

Conflicts of interest

There are no conflicts of interest to declare.

Acknowledgements

Notes and references

1 F.-S. Guo, B. Day, Y.-C. Chen, M.-L. Tong, A. Mansikamäkki and R. A. Layfield, *Angew. Chem., Int. Ed.*, 2017, **56**, 11445; C. A. P. Goodwin, F. Ortu, D. Reta, N. F. Chilton and D. P. Mills, *Nature*, 2017, **548**, 439.

2 Y.-S. Ding, N. F. Chilton, R. E. P. Winpenny and Y.-Z. Zheng, *Angew. Chem., Int. Ed.*, 2016, **55**, 16071.

3 S. K. Gupta, T. Rajeshkumar, G. Rajaraman and R. Murugavel, *Chem. Sci.*, 2016, **7**, 5181.

4 J. Liu, Y.-C. Chen, J.-H. Jia, J.-L. Liu, V. Vieru, L. Ungur, L. F. Chibotaru, Y. Lan, W. Wernsdorfer, S. Gao, X.-M. Chen and M.-L. Tong, *J. Am. Chem. Soc.*, 2016, **138**, 5441.

5 M. Gregson, N. F. Chilton, A.-M. Ariciu, F. Tuna, I. F. Crowe, W. Lewis, A. J. Blake, D. Collison, E. J. L. McInnes, R. E. P. Winpenny and S. T. Liddle, *Chem. Sci.*, 2016, **7**, 155.

6 N. Domingo, E. Bellido and D. Ruiz-Molina, *Chem. Soc. Rev.*, 2012, **41**, 258.

7 S. Thiele, F. Balestro, R. Ballou, S. Klyatskaya, M. Ruben and W. Wernsdorfer, *Science*, 2014, **344**, 1135.

8 C. Wäckerlin, F. Donati, A. Singha, R. Baltic, S. Rusponi, K. Diller, F. Patthey, M. Pivetta, Y. Lan, S. Klyatskaya, M. Ruben, H. Brune and J. Dreiser, *Adv. Mater.*, 2016, 5142.

9 E. Moreno Pineda, T. Komeda, K. Katoh, M. Yamashita and M. Ruben, *Dalton Trans.*, 2016, **45**, 18417.

10 J. A. J. Burgess, L. Malavolti, V. Lanzilotto, M. Mannini, S. Yan, S. Ninova, F. Totti, S. Rolf-Pissarczyk, A. Cornia, R. Sessoli and S. Loth, *Nat. Commun.*, 2015, **6**, 8216.

11 M. Mannini and A. Cornia, in *Molecular Nanomagnets and Related Phenomena*, ed. S. Gao, Springer, 2015, pp. 293–330.

12 L. Sorace and D. Gatteschi, in *Lanthanides and Actinides in Molecular Magnetism*, ed. R. A. Layfield and M. Murugesu, Wiley, 2015, pp. 1–25.

13 Y. C. Chen, J. L. Liu, L. Ungur, J. Liu, Q. W. Li, L. F. Wang, Z. P. Ni, L. F. Chibotaru, X. M. Chen and M. L. Tong, *J. Am. Chem. Soc.*, 2016, **138**, 2829.

14 S. T. Liddle and J. van Slageren, *Chem. Soc. Rev.*, 2015, **44**, 6655.

15 J. Long, B. G. Shestakov, D. Liu, L. F. Chibotaru, Y. Guari, A. V. Cherkasov, G. K. Fukin, A. A. Trifonov and J. Larionova, *Chem. Commun.*, 2017, **53**, 4706.

16 D. N. Woodruff, R. E. P. Winpenny and R. A. Layfield, *Chem. Rev.*, 2013, **113**, 5110.

17 P. Zhang, Y.-N. Guo and J. Tang, *Coord. Chem. Rev.*, 2013, **257**, 1728.

18 H. L. C. Feltham and S. Brooker, *Coord. Chem. Rev.*, 2014, **276**, 1; S. G. McAdams, A.-M. Ariciu, A. K. Kostopoulos, J. P. S. Walsh and F. Tuna, *Coord. Chem. Rev.*, 2017, **346**, 216.

19 J. D. Rinehart and J. R. Long, *Chem. Sci.*, 2011, **2**, 2078.

20 F. Pointillart, K. Bernot, S. Golhen, B. Le Guennic, T. Guizouarn, L. Ouahab and O. Cador, *Angew. Chem., Int. Ed.*, 2015, **54**, 1504.

21 R. Sessoli and A. K. Powell, *Coord. Chem. Rev.*, 2009, **253**, 2328.

22 F. Habib and M. Murugesu, *Chem. Soc. Rev.*, 2013, **42**, 3278.

23 L. F. Chibotaru, L. Ungur and A. Soncini, *Angew. Chem., Int. Ed.*, 2008, **47**, 4126.

24 F. Habib, G. Brunet, V. Vieru, I. Korobkov, L. F. Chibotaru and M. Murugesu, *J. Am. Chem. Soc.*, 2013, 2.

25 G.-F. Xu, Q.-L. Wang, P. Gamez, Y. Ma, R. Clérac, J. Tang, S.-P. Yan, P. Cheng and D.-Z. Liao, *Chem. Commun.*, 2010, **46**, 1506.

26 K. L. M. Harriman, J. J. Le Roy, L. Ungur, R. Holmberg, I. Korobkov and M. Murugesu, *Chem. Sci.*, 2017, **8**, 231.

27 H.-M. Dong, H.-Y. Li, Y.-Q. Zhang, E.-C. Yang and X.-J. Zhao, *Inorg. Chem.*, 2017, **56**, 5611.

28 J. D. Rinehart, M. Fang, W. J. Evans and J. R. Long, *J. Am. Chem. Soc.*, 2011, **133**, 14236.

29 S. Demir, J. M. Zadrozny, M. Nippe and J. R. Long, *J. Am. Chem. Soc.*, 2012, **134**, 18546.

30 F.-S. Guo and R. A. Layfield, *Chem. Commun.*, 2017, **53**, 3130.

31 F. Pointillart, B. Le Guennic, S. Golhen, O. Cador and L. Ouahab, *Chem. Commun.*, 2013, **49**, 11632.

32 S. Demir, I.-R. Jeon, J. R. Long and T. D. Harris, *Coord. Chem. Rev.*, 2015, **289–290**, 149.

33 B. Dolinar, S. Gómez-Coca, D. Alexandropoulos and K. R. Dunbar, *Chem. Commun.*, 2017, **53**, 2283.

34 C. Carbonera, A. Dei, J.-F. Létard, C. Sangregorio and L. Sorace, *Angew. Chem., Int. Ed.*, 2004, **43**, 3136.

35 J. Tao, H. Maruyama and O. Sato, *J. Am. Chem. Soc.*, 2006, **128**, 1790.

36 M. Abdus Subhan, R. Kawahata, H. Nakata, A. Fuyuhiro, T. Tsukuda and S. Kaizaki, *Inorg. Chim. Acta*, 2004, **357**, 3139.

37 M. Cano, J. V. Heras, E. Santamaria, E. Pinilla, A. Monge, J. J. Cristopher and J. A. Mccleverty, *Polyhedron*, 1993, **12**, 1711.

38 A. Paulo, J. Ascenso, Â. Domingos and I. Santos, *Dalton Trans.*, 1999, 1293.

39 M. J. Saly, J. Li, M. J. Heeg and C. H. Winter, *J. Am. Chem. Soc.*, 2011, 10.

40 D. Casanova, M. Llunell, P. Alemany and S. Alvarez, *Chem. – Eur. J.*, 2005, **11**, 1479.

41 M. Llunell, D. Casanova, J. Cirera, J. M. Bofill, P. Alemany, S. Alvarez, M. Pinsky and D. Avnir, *SHAPE 2.0*, Universitat de Barcelona and The Hebrew University of Jerusalem, Barcelona, 2003.

42 M. A. J. Moss and C. J. Jones, *J. Chem. Soc., Dalton Trans.*, 1990, 581.

43 N. G. Connelly, Royal Society of Chemistry (Great Britain) and International Union of Pure and Applied Chemistry, in *Nomenclature of inorganic chemistry. IUPAC recommendations 2005*, Royal Society of Chemistry, 2005.

44 S. Kitagawa, *Coord. Chem. Rev.*, 2002, **224**, 11.

45 A. S. Gajadhar-Plummer, I. A. Kahwa, A. J. P. White and D. J. Williams, *Inorg. Chem.*, 1999, **38**, 1745.

46 J. Wu, L. Zhao, M. Guo and J. Tang, *Chem. Commun.*, 2015, **51**, 17317.

47 D. Guo and J. K. McCusker, *Inorg. Chem.*, 2007, **46**, 3257.

48 A. Vogler and H. Kunkely, *Inorg. Chim. Acta*, 2006, **359**, 4130.

49 W. T. Carnall, P. R. Fields and K. Rajnak, *J. Chem. Phys.*, 1968, **49**, 4424.

50 F. Marken, A. Neudeck and A. M. Bond, in *Electroanalytical Methods*, Springer Berlin Heidelberg, Berlin, Heidelberg, 2005, pp. 51–97.

51 F. E. Mabbs and D. Collison, *Electron paramagnetic resonance of d transition metal compounds*, Elsevier, 1992.

52 A. Caneschi, A. Dei, D. Gatteschi, C. A. Massa, L. A. Pardi, S. Poussereau and L. Sorace, *Chem. Phys. Lett.*, 2003, **371**, 694.

53 N. F. Chilton, R. P. Anderson, L. D. Turner, A. Soncini and K. S. Murray, *J. Comput. Chem.*, 2013, **34**, 1164.

54 R. L. Carlin, *Magnetochemistry*, Springer-Verlag, 1986.

55 M. J. Martı, O. Roubeau, D. Zueco, P. J. Alonso, M. Evangelisti, F. Luis and A. Repolle, *Phys. Rev. Lett.*, 2011, **107**, 117203.

56 P.-E. Car, M. Perfetti, M. Mannini, A. Favre, A. Caneschi and R. Sessoli, *Chem. Commun.*, 2011, **47**, 3751.

57 S. Xue, L. Ungur, Y. Guo, J. Tang and L. F. Chibotaru, *Inorg. Chem.*, 2014, **53**, 12658.

58 E. Lucaccini, M. Briganti, M. Perfetti, L. Vendier, J. Costes, F. Totti, L. Sorace and R. Sessoli, *Chem. – Eur. J.*, 2016, **22**, 5552.

59 D. Gatteschi, R. Sessoli and J. Villain, *Molecular Nanomagnets*, Oxford University Press, 2006.

60 E. Lucaccini, L. Sorace, M. Perfetti, J.-P. Costes and R. Sessoli, *Chem. Commun.*, 2014, **50**, 1648.

61 Y. Rechkemmer, J. E. Fischer, R. Marx, M. Dörfel, P. Neugebauer, S. Horvath, M. Gysler, T. Brock-Nannestad, W. Frey, M. F. Reid and J. van Slageren, *J. Am. Chem. Soc.*, 2015, **137**, 13114.

62 M. Vonci, M. J. Giansiracusa, R. W. Gable, W. Van den Heuvel, K. Latham, B. Moubaraki, K. S. Murray, D. Yu, R. Mole, A. Soncini and C. Boskovic, *Chem. Commun.*, 2016, **52**, 2091; M. Vonci, M. J. Giansiracusa, R. W. Gable, W. Van den Heuvel, B. Moubaraki, K. S. Murray, D. Yu, R. A. Mole, A. Soncini and C. Boskovic, *Inorg. Chem.*, 2017, **56**, 378.

63 A. Amjad, A. M. Madalan, M. Andruh, A. Caneschi and L. Sorace, *Chem. – Eur. J.*, 2016, **22**, 12849.

64 F. Kögl and A. Lang, *Ber. Dtsch. Chem. Ges.*, 1926, **59**, 910.

65 S. Trofimenko, *J. Am. Chem. Soc.*, 1967, **89**, 3170.

66 M. Abdus Subhan, R. Kawahata, H. Nakata, A. Fuyuhiro, T. Tsukuda and S. Kaizaki, *Inorg. Chim. Acta*, 2004, **357**, 3139.

67 W. Kabsch, *Acta Crystallogr., Sect. D: Biol. Crystallogr.*, 2010, **66**, 125.

68 G. M. Sheldrick, *SADABS. University of Göttingen*, Germany, 1996.

69 G. M. Sheldrick, *Acta Crystallogr., Sect. A: Fundam. Crystallogr.*, 2015, **71**, 3.

70 G. M. Sheldrick, *Acta Crystallogr., Sect. C: Cryst. Struct. Commun.*, 2015, **71**, 3.